Marine Structures 78 (2021) 102943

Contents lists available at ScienceDirect

Marine Structures

journal homepage: www.elsevier.com/locate/marstruc

Experimental investigation of structural system capacity with multiple fatigue cracks

Kaihua Zhang, Matthew Collette *

Department of Naval Architecture and Marine Engineering, University of Michigan, Ann Arbor, MI, United States of America

ARTICLE INFO

Keywords:
Fatigue test
Laboratory scale
Multi-degradation
Marine structures
Crack length measurement

ABSTRACT

Few experimental data sets exist in the literature to support the development and evaluation of digital twins predicting structural degradation. The literature is especially sparse for system tests where multiple failures occur and interact. In this work, a laboratory-level experiment is conducted to mimic many of the properties of larger and more complex marine structures with redundant load paths, failure interaction, and component-to-system level integration. In the experiment, such properties are reflected by a hexagon tension specimen with four propagating fatigue cracks tested under displacement-controlled loading. The applied loading cycles and corresponding crack lengths are recorded as the major time-varying data of degradation, with the resisting force at maximum extension used as the system capacity. A novel computer vision method is used to measure the crack length. Strain gauges are also used to monitor the structure's status. The experimental data is presented and analyzed in this paper. The resulting data sets can be used to evaluate the performance of different digital twin updating approaches.

1. Introduction

Digital twin approaches combine numerical models, observations, and sensor input to provide prognosis on the future capability of marine systems. Such twins have been widely discussed as a means of improving both performance and safety. Their popularity is growing as the cost of sensing, computing, and artificial intelligence required for a twin have been reduced. For structural systems, such twins are an attractive way of optimally scheduling maintenance and repair. However, very little experimental data exists to guide the development and validation of such efforts. Previous studies in the field have mainly relied on synthetic or numerical data to simulate the degradation of the structural system. Additionally, much of the previous work in this space addresses only single failures in isolation, ignoring the potential for interacting failures in complex structural systems. This work presents a laboratory scale experiment of a hexagon-shaped specimen with four propagating fatigue cracks. While not physically representative of a ship fatigue-critical detail, this specimen is designed to mimic many of the system properties of degrading marine structures in a cost-effective format. The hexagon design features crack-to-crack interaction, component interdependence, redundant load path and non-binary failure states, all characteristics of a full-scale marine structure undergoing fatigue degradation. The design of specimen, methods of measuring crack length, experimental set-up, and the collected data are presented and discussed.

The marine structures community has a long history of probabilistic risk-based inspection strategies and model updating, and these have provided the foundation for digital twin approaches. To date, most of this work has focused around load updating, corrosion and structural fatigue cracking. Fatigue cracking, with the potential for fracture or loss of structural capacity has long been a central problem for aging structures [1]. While fatigue cracks in locations that could lead to catastrophic collapse require

* Corresponding author.
E-mail address: mdcoll@umich.edu (M. Collette).

https://doi.org/10.1016/j.marstruc.2021.102943
Received 13 May 2020; Received in revised form 11 January 2021; Accepted 16 January 2021
Available online 27 April 2021

immediate repair, repair urgency for cracks in less critical locations is not clear and previous authors have examined cost and risk optimal strategies for scheduling such repairs [2]. Thus, the ability to predict the evolution of such damage over time, and the likely crack size in the future is key to determining the repair strategy.

Recent work in fatigue has highlighted the desire for such probabilistic updating methods. Lotsberg et al. provide an overview of inspection updating on single fatigue cracks in a probabilistic framework [3]. Abbas and Shafiee [4] provide a recent review paper covering progress in corrosion updating and inspection techniques. Straub [5] proposed a Dynamic Bayesian Network approach for monitoring and prognosis for fatigue cracks, this approach has since been coupled to load updating by the present authors [6,7]. Straub's group then extended these methods to system-level performance metrics and inspection planning, including a study on the Zayas offshore structure benchmark frame [8,9]. Cai et al. [10] looked at combining multiple environmental factors into pipeline reliability, while Liu et al. [11] provided a system-level optimization for service life extension of a naval vessel structural systems. These recent papers show that there is a strong interest in developing prognosis systems for marine structures undergoing degradation. However, none of the papers used actual experimental data to evaluated their proposed prognosis techniques. Instead, most authors generated synthetic numerical data which they used to evaluate their methods. Thus, the true performance of such techniques on actual structural systems is hard to assess at the present and making a laboratory-scale test data set to support such assessments seems valuable.

In the past decades, experimental tests of marine structures have been conducted in several sub-areas. The most common tests focus on the components of marine structures, determining the component strength and properties. Numerous component experiments can be found in the literature, including compressive and collapse tests on stiffened panels [12,13], strength analysis on deteriorated steels plates [14,15], and fatigue evaluation on welded ship structural joints [16]. Experiments of single components do not consider critical properties of real-world complex structural system such as the interdependence of components. Some larger experiments are also conducted with less frequency, including the assessment of corroded box-girders [17,18]. However, the cost and time required makes such testing expensive; especially at large scale.

Likewise, tracking multiple cracks in a large structure is expensive owing to the size of the structure necessary. Most the multi-crack work published to date have focused on multiple cracks growing near enough that there is direct interaction between the crack stress fields and often the crack themselves. Pang et al. [19] examined coalescing fatigue cracks in pipeline joints, while Anis et al. [20] proposed simplified stress field estimations for multiple cracks propagating near each other. Sun et al. [21] applied similar methods to a cutting head on a tunnel boring machine. These publications only cover part of the problem of interest in marine structures, where the growth of multiple cracks changes the structure's behavior without direct interaction between the crack tips.

However, marine multi-crack examples are even rarer, with few publications over the last two decades. Guedes Soares and Garbatov [22] formulated the reliability problem for structural systems undergoing both multiple crack growth and corrosion, but the crack models were simple and did not interact. Okawa, Sumi, and Mohri [23] examined multiple cracks in a stiffened panel, but the majority of the cracks initiated from the same location before growing into different members. More recently, Huang et al. [24] looked at reliability at the web-frame joint with multiple correlated fatigue initiation sites, but no crack growth was modeled. A crack-growth extension was proposed by Huang and Sridhar [25], looking at reliability with inspection updating. These recent developments come closest to providing a multi-crack digital twin framework, however no experimental validation of these approaches has yet been published.

Thus, a laboratory scale experiment reflecting many of the properties of large and complex marine structures would be a major advantage in developing and testing digital twin approaches. The designed experiment should not only mimic multiple degradation processes to explore the interactions among components, but also retain structural redundancy so that a single component failure will not remove all load carrying capacity.

This paper presents a laboratory-scale experiment of a specimen with multiple simultaneous degradation sites to mimic the properties of complex marine structural systems. The goal of the experiment is to collect data reflecting real world marine structures with a cost-effective and time-efficient experiment. The details of the experimental design, including the design of the specimen, the development of the crack measurement methods and strain gauge monitoring are presented in Section 2. Section 3 contains the experimental results with crack length measured by the developed methods. The performance of developed methods and the results of strain gauge monitoring are also included in Section 3. Conclusions can be found in Section 4.

2. Experimental design

2.1. Specimen design and test logic

The primary goal of the experimental design is to come up with a laboratory-scale specimen that can recreate many of the system properties of a full-scale marine structure. By keeping the experiment at lab scale, the cost and time associated with the test will be significantly reduced. Thus, while the specimen does not physically match any marine structure of interest, it should reflect several system-level properties of more complex marine structures, including:

- Multiple components with redundant load paths.
- Degrading structural health over the course of the experiment.
- Degrading through a relevant physical mechanism for a full-scale structure.
- Failures that are continuous, not binary states of intact or completely failed

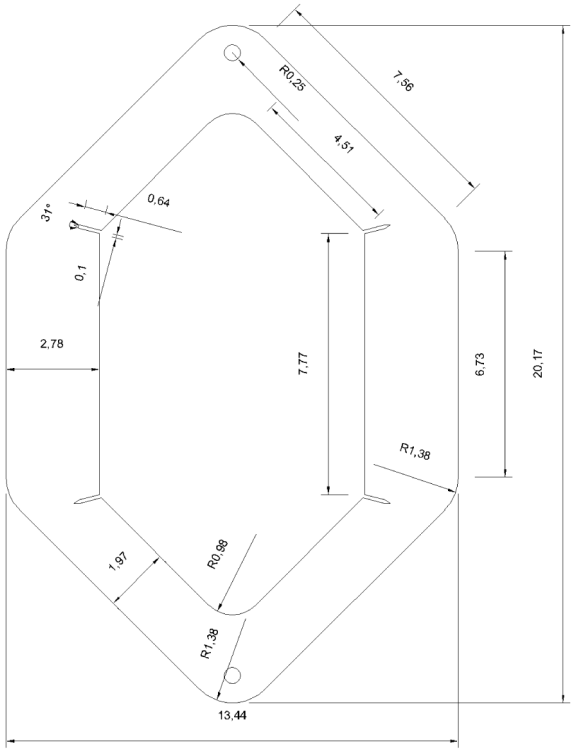

Fig. 1. Plot of hexagon specimen, dimensions in inches.

- Failures that can interact so that the degradation can evolve in several different ways.
- Allowing for efficient periodic inspections by several different methods.
- Contains a common system-level parameter to measure overall structural performance.

After brainstorming, a hexagon-shaped multi-crack fatigue specimen design was selected to best meet the properties listed above. The specimen is shown in Fig. 1. In this approach four propagating cracks are introduced, one at each end of the straight bar on each side of the specimen. These cracks grow throughout the experiment under displacement-controlled tensile loading applied through the bolt holes at the extreme top and bottom of the specimen. The cracks interact with each other, as under displacement control, a large crack on one side of the specimen will shield the second crack on the same side by reducing the stiffness of, and load in, that side of the specimen. There is redundancy in that even with a complete failure of a single side, the specimen can still resist loading. The fatigue crack growth provides both a relevant physical degradation mechanism, and one that is straightforward to gather data from crack length measurements. Finally, the maximum resisting tensile force at the maximum applied displacement is used as a metric of the overall system capacity. This capacity metric will degrade over time as the specimen becomes more compliant as the cracks grow. By starting all cracks at approximately the same size, a system-level twin challenge is introduced; the twin must be able to predict the future evolution of each crack, including crack–crack interactions, to correctly predict future system capacity.

The hexagon structure was designed with four starter notches, based on ASTM standard E1820 with 15 degree orientation. The 15 degree initial angle allows the crack growth to be approximately straight throughout the experiment. A plot of the design is shown in Fig. 1 with dimensions in inches. Except for the four corners where starter notches are located, the other corners are rounded to reduce stress concentrations. The frames of the hexagon specimen without starter notches were cut by waterjet cutting from sheets of ASTM A36 steel.

The starter notches were machined by wire electrical discharge machining (EDM) with a 0.1 mm diameter wire to make a high-resolution starting notches, their initial length was approximately 20.5 mm, with about 4 mm of EDM starter notches and the remainder a waterjet-cut slot. An Abaqus model was built to find the required displacement and reaction force with respect to the desired stress intensity factor. Quadratic elements C3D20 were used for the frame while C3D15 elements were employed for modeling the crack front. Under 0.65 mm maximum displacement, the maximum reaction force is 22.05 kN and the stress intensity factor is 31.8 $\text{MPa}\sqrt{m}$, which is capable of initiating stable crack propagation from the starter notch (see Fig. 2).

In addition to the specimen, two grips were designed to mount the specimen onto the fatigue test machine. For ease of fabrication, these were assembled from a head component and a threaded stud component. By connecting the threaded stud component with the head component, the stress concentration at the transition from the head to the thread is reduced compared to a monolithic mount. At assembly, this connection was fastened by Loctite Threadlocker Red 271. Fig. 3 shows a 3D sketch of the grip. The thread

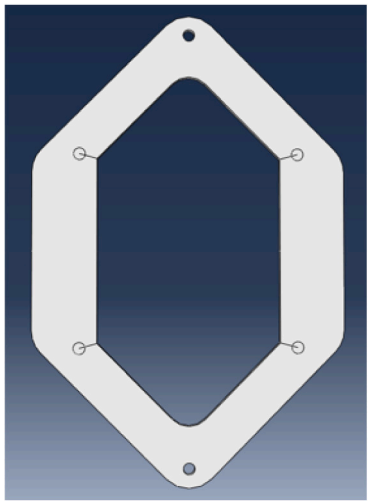

Fig. 2. ABAQUS model of hexagon specimen with four initial cracks.

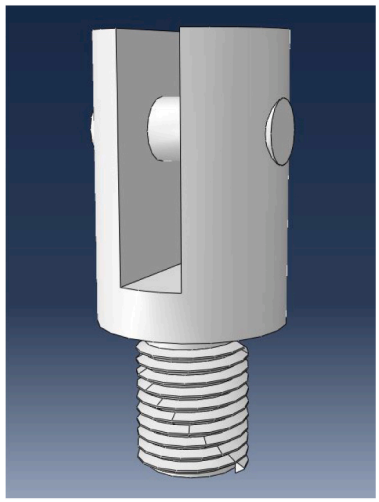

Fig. 3. 3D sketch of grip.

stub fastens the grip onto the test machine while a bolt going through the head component locks the specimen and grip together. The head component was machined from 1215 carbon steel; the thread stud was made from B7 alloy steel, and the hex bolt was selected as grade 8 bolts with a zinc plated surface. Two 1.6 mm thick polyvinyl chloride (PVC) washers are placed between the specimen and grip to center the specimen and ensure the generated tensile load is in the plane of the hexagon.

An MTS 810 material testing system, a multipurpose servohydraulic testing systems with 250 kN capability and ±75 mm stroke, was selected for performing the test. Fig. 4 shows the MTS 810 material testing system mounted with the hexagon specimen.

Owing to the symmetric shape, the four starter notches are equivalent at the beginning of the experiment but one or two cracks are expected to be dominant with increasing cycles. The specimen encourages this behavior as the nominal stress is the same on each side of the specimen. Thus if one crack on a side starts to grow a little faster, its stress intensity factor will increase, further increasing its growth rate and causing it to pull away from the other crack on the same side. Thus, the specimen is inherently unstable to small variations in crack growth. This instability, plus the dependence of the nominal stress on each side of the specimen on both crack lengths on that side of specimen introduces complex interactions among the cracks. The specimen is loaded in tensile cycles with a constant maximum displacement, and the reaction force at the maximum displacement is treated as a stand-in for the overall system capability of the structure. This force reduces over time as the cracks grow. The data gathered from the experiment are the number of applied cycles versus corresponding maximum reaction force and crack length.

In total, five hexagon specimens were investigated in this work. The first had starter notches that were perpendicular to the vertical bars of the hexagon, and as result, the propagating crack emerged at an angle to the starter notches. The remaining four had angled starter notches with no visible difference in crack propagation direction from the starter notches. Table 1 below gives the

Fig. 4. Setup of hexagon specimen with MTS 810 material testing system.

Table 1
Test plan with data sources collected on each test.

Specimen	Pre-load	Defl. amp.	Max. load	React. force	Crack length			Strain gauge
	kN	mm	kN		Scale	DIC	CV	
1	8.6	0.25	23.44	X	X	–	–	–
2	9.69	0.25	22.16	X	X	X	X	–
3	12	0.25	24.07	X	X	–	–	X
4	9.1	0.25	21.61	X	X	X	X	X
5	9.3	0.25	21.77	X	X	X	X	X

parameters and measuring systems used on each specimen. These tests were carried out under positive, but varying, R-ratio owing to the displacement control. After applying the pre-load, the resulting position was taken as the minimum displacement for the test. Then sinusoidal displacements with amplitude of 0.25 mm (0.5 mm peak-to-trough) were used during the test. Specimen five will be primarily discussed here. Summary data for all the remaining specimens is included in an Appendix to this paper. Additionally, full experimental details and data sets have been archived in the University of Michigan Library's archive service Deep Blue in the first author's PhD Thesis [26], and the corresponding data repository https://doi.org/10.7302/e3n8-wa61.

2.2. Crack measurement

2.2.1. Overview and previous work

To gather crack lengths from the experiment, three methods were used in this study: visually using a machinist scale, a novel computer vision method and a digital image correlation (DIC) method. Usually, measuring crack length with a machinist scale by eye is not accurate enough, especially for cracks with curvature. Thus, the computer vision and DIC methods are developed and explored for a more accurate measurement for this type of multi-crack specimen.

During the past decades several different methods for measuring crack lengths and widths have been proposed. The most conventional method is a crack width gauge which is a scale containing a transparent upper plate marked with a red crosshair cursor and a white bottom plate marked with measuring grid. The distance between cursor and grid indicates the width of the crack. However, this method is designed commonly for measuring crack width restricting its usage in measuring crack length; and an error is introduced by observing the crack optically. Extending from the idea of a crack width gauge, a traveling microscope can also be used for measuring crack length. Traveling microscopes consist of a fixed base holding a movable microscope. The microscope can reduce the optical error in determining the crack tip location by using high magnification. It successfully monitored the fatigue crack propagation in polymer foams [27]. However, in the present multi-crack application, this approach requires either removing the specimen from the testing machine for measurement, or re-positioning the microscope to the location of each crack. If the crack grows in an unexpected direction incompatible with the initial mounting, the mounting must be changed during the experiment. Neither of these approaches would be efficient for a multi-crack specimen like the hexagon tested here. Several other techniques have been developed involving acoustic wave reflection. Acoustic wave methods use a transmitter and a receiver sending and receiving acoustic waves at a specific frequency [28–30]. The high-frequency component of the transmitted wave will be reflected from any discontinuities in the structure such as cracks and flaws. However, the complexity of the technology and specialized knowledge required to implement this technique limit the application in experiments.

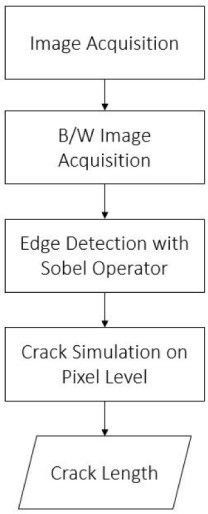

Fig. 5. Flow chart of crack length measuring process based on computer vision.

Benefiting from the recent advances in digital cameras and computer vision technologies, digital image processing has emerged as a low-cost and easy-to-use methods for characterizing cracks. Such techniques have been widely explored in civil engineering. Detecting cracks with computer vision has been explored by a histogram-based classification algorithm [31] and a K-Means clustering method [32]. Machine vision has also been employed in structural reconstruction to obtain depth perception and detect cracks [33,34]. For measuring the crack length on large concrete structures, robotic systems have developed for detecting and tracing cracks in bridge inspection [35,36]. The images are collected by a ground-based robot and the crack properties are extracted for further analysis; however, this method requires a user to decide the start and end points of crack manually which could introduce error for our application. Compared to detecting and measuring cracks on concrete in civil engineering area, the cracks on steel structures are often harder to see visually, making the current application a more challenging computer vision problem. However, developing an image-based crack measuring method for steel structures would provide a rapid and easy-to-use means for conducting crack measurements on multi-crack experimental such as hexagon considered here. Given the small width of steel cracks, the developed technique is currently targeted for laboratory specimens, where lighting, corrosion, dirt, paint and similar complicating factors can be closely controlled. For *in-situ* applications on full-scale structures in service, a means for adjusting for such factors would need to be developed.

In addition to raw computer vision technologies, the DIC method, as an analysis method of multiple digital images, has been explored in monitoring cracks. DIC is capable of estimating the displacement field in a continuous specimen. This field, and the associated strain and stress fields, can be used to locate the tips of propagating cracks [37,38]. DIC has also been used to perform full-field measurement to explore the crack growth behavior of functionally graded materials [39]. Inspired by these applications, the DIC method was also used to acquire the strain field and locate the crack tip in this application.

2.2.2. Computer vision based method

A new computer vision (CV) method for measuring cracks was implemented in this work. The computer vision method takes a digital image of a specimen with an embedded crack, and attempts to identify and measure the crack length on the level of individual pixels in the image. Fig. 5 shows the procedure of applying this method. The first step is acquiring crack images with one or more digital cameras, which store RGB images with the amount of red, green and blue colors at each pixel point. Since the colors are not helpful for detecting cracks, the RGB image is transferred to a 256-bit grayscale image and pre-processed with Gaussian filter in the second step. The pixel values in the grayscale image indicate the amount of light at that pixel ranging from 0 (black) to 255 (white). In the third step, a Sobel operator is applied for detecting the cracks on the smoothed grayscale image. Then noise is filtered out for a more accurate calculation of crack length on pixel level. The last step is transferring the pixel-level crack length to the real dimension in millimeters using the length of a known feature in the image. The method is semi-automated, and proved capable of making rapid crack length measurements for multiple cracks.

Image acquisition

A GoPro HERO4 camera with 12.0 Mega Pixel (MP) resolution is used to take JPEG pictures at a 4000 × 3000 pixel resolution. A NEEWER 12.5X macro lens is mounted on the GoPro camera to focus on the small region around a growing crack. The camera is mounted on a flexible tripod that can be easily moved around a specimen to take images of all active cracks. The setup for capturing images is shown in Fig. 6. In order to increase the contrast between the structure surface and the crack, the crack area is painted with a fluid fluorescent dye showing a bright maize color under ultraviolet (UV) lights. The UV dye is painted on the surface of

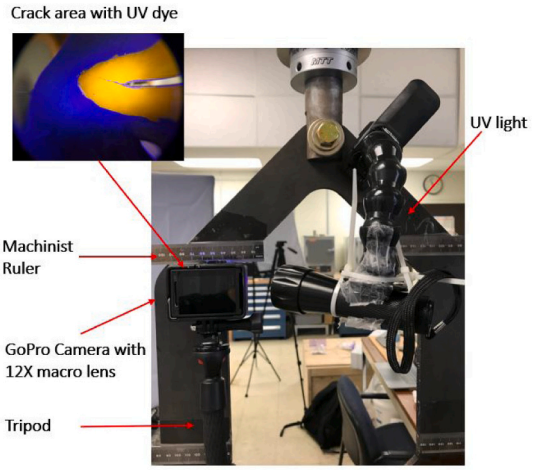

Fig. 6. Setup of image capture for computer vision method.

the structure when the crack is closed by removing the loading on the structure (e.g. pausing the fatigue test apparatus at zero or a low load value). After the crack is re-opened by re-applying load to the specimen, the dye makes the crack opening clearer in the image.

Image pre-processing

After capturing images, several pre-processing techniques are applied to prepare the images for crack detection. The first pre-processing step for the images is transferring the RGB image to grayscale for the convenience of applying filters. In this step, the color information in the image is replaced by the amount of light or intensity at each pixel. Then, a Gaussian filter is implemented as the second pre-processing step to smooth the image and reduce the amount of noise in the image. This filter can enhance the image quality captured under poor or uneven lighting. The Gaussian filter is implemented as a window moving along the pixels, convolving each pixel values with a Gaussian function. The Gaussian function in two dimensions is shown in Eq. (1), where x is the coordinate in the horizontal axis, y is the coordinate in the vertical axis and σ is the standard deviation of the Gaussian distribution [40,41]. Values are sampled from Eq. (1) to build a convolution matrix which is applied to the grayscale image.

$$G(x,y) = \frac{1}{2\pi\sigma^2} e^{-\frac{x^2+y^2}{2\sigma^2}} \tag{1}$$

Edge detection

In order to detect cracks, a Sobel operator is applied to the processed image. The Sobel operator is a gradient operator approximating the gradient of the image density. Cracks corresponding to high spatial variability in image intensity can be captured by the Sobel operator. The Sobel operator is composed of two convolution matrices applied on the horizontal and vertical directions. The two matrices measure the gradient in each orientation of the input image which can be combined following Eq. (2) to calculate the gradient magnitude at each pixel. In Eq. (2), G_x is the gradient in the horizontal direction while G_y is the vertical gradient. In implementation, the Sobel operator convolves the image with a integer-valued filter in the horizontal and vertical directions.

$$|G| = \sqrt{(G_x^2 + G_y^2)} \tag{2}$$

Crack simulation and calculation

The crack images usually contains some noise as well as the crack image, which can make determining the crack path difficult. Therefore, it is critical to filter out noise before calculating crack length. At this point in the process, the image has been transformed into a matrix of gradient values. The gradient from the Sobel operator is first filtered by a fixed threshold. This eliminates points with relatively small gradients as experience shows that the crack edge should be accompanied by obvious an intensity change and thus a relatively large gradient magnitude. The threshold can be set higher for a higher-quality image compared with poorer quality images. Additionally the Sobel operator can also detect the boundaries of an image so the gradients near boundaries are set to 0.

After the noise filter, the image will still contain some regions of higher gradients that are not part of the crack which may come from non-uniform lighting or uneven painting. In the images taken in this study, the cracks run primarily horizontally across the image, and thus the crack itself is marked by a series of consecutively high gradient values in each column of the gradient matrix. This series of high gradient values in a specific column indicates the width of the crack at the specific location in the image. Some noise points have the similar format but less "width", or consecutive rows with high gradient values, than the real continuous cracks. These noise points are filtered out according to their short width, and the corresponding lower number of rows. It is observed that noise points usually cover less than three rows which is adopted as the threshold for filtering out noise points with short width. Both

the threshold and width filtering steps depend on the resolution of the image and image quality, and would need to be adjusted for each type of test and camera. However, once tuned, these parameters allowed a robust detection of the crack path.

After filtering out noise points at the pixel level, the next step is calculating the crack length at the pixel level. The filtered numerical values at each original pixel point now refers to the gradient magnitude. The length calculation requires tracing along the locations of pixel points whose gradient magnitude is significant. Since crack width is not considered in calculating crack length, each column of sequentially numerically-large gradients indicating the crack are compressed vertically by selecting the median of their coordinate locations. The median is used instead of mean to avoid bias from any possible outliers in each column. A series of pixel points coordinates is acquired in this step representing the location of the crack across the image. Calculating the crack length based on every pixel point can introduce bias as there may be some noise in the vertical median location which would make overall length calculations difficult. Thus, ten pixel points are compressed and grouped together horizontally by selecting the median of the grouped pixel points. The resulting points are then used for a Euclidean calculation of crack length at the pixel level. In summary, the gradient magnitudes are compressed vertically first since crack width is not considered for calculating crack length, then the magnitudes are compressed horizontally for representing the crack length accurately.

The last step is transferring the pixel length to a real world dimension in millimeter. Here, a feature in the image of known size is needed to establish a relationship between pixels and real-world distance. For this step, the quality of the initial image is also critical, as the image sensor must be parallel to the surface of the specimen, and areas of high lens distortion must be avoided. In trials to date, a simple machinist scale glued on the specimen bridges the dimension in millimeters and pixel length finishing the calculation of crack length. The scale is marked down to 0.5 mm resolution, and be located immediately adjacent to the crack to establish this conversion.

In summary, the computer vision method developed is a rapid and simple method to measure crack length. It requires painting the crack area with a contrast-enhancing dye under no load, and taking an image under a load sufficient to open the crack. The image processing procedure does require some tuning for lighting conditions and the camera used, but once these parameters were established, the method provided consistent crack length estimations. For a test like the hexagon tests here, where many crack length measurements are required at multiple locations on the same specimen, it proved a practical and efficient method.

2.2.3. Validation of computer vision based method

As the proposed computer vision method was new, it was essential to validate it before using it on the hexagon experiments. Two standard eccentrically-loaded single edge crack tension specimens [42] were tested on an MTS 810 testing system to perform this validation. The detailed dimensions are shown in the specimen plot, Fig. 7. The specimen without starter notches was cut by waterjet from an A36 steel sheet and then each starter notch was machined by wire EDM with 0.1 mm diameter wire for high-resolution crack tips. The standard specimens were preloaded at 8 kN to guarantee a slack-free connection between the specimen and the fixture bolts. The tests were conducted under displacement control with a maximum displacement amplitude of 0.14 mm resulting to a maximum reaction force of 23.6 kN. An Abaqus model was built to calculate the stress intensity factor given specific displacements. The detail procedure is similar to the modeling of the hexagon specimen in Section 2.1. The calculated stress intensity factor is 30 MPa$\sqrt{m}$ with 23.6 kN maximum reaction force under 0.3 mm of total displacement. Crack lengths were recorded at six different points during the first test, while eleven crack length measurements were gathered during the second test.

To provide a basis for comparison, a traveling microscope is employed to measure the crack length on the back side of the specimen while the new computer vision method measures the crack on the front side. The microscope has 20X magnification capability and is equipped with a micrometer with a resolution of $1e^{-5}$ inches. To help the traverse microscope locate the crack tip, UV dye is also painted on the backside surface of the specimen when the crack is closed by pausing the fatigue test apparatus at zero or a low load value. After the crack is re-opened by re-applying load to the specimen, the crack length is measured. The measured crack length is compared with the results from the CV method. In order to ensure the cracks on both sides are identical, a machinist scale with marking of 0.5 mm was also used to measure the crack length on the front to compare with the microscope. These readings showed that the crack front was generally straight through the thickness of the material. The setup of the validation test is shown in Fig. 8.

Fig. 9 demonstrates the application of the developed CV method on the captured crack images. To increase the contrast between the crack and the structure's surface, the UV dye is painted after the testing machine is temporarily stopped resulting in no applied displacement on the specimen. Then the specimen is subjected to the maximum displacement to open the crack as shown in Fig. 9(a) as the original image, which is transferred to grayscale in Fig. 9(b). The grayscale image is smoothed by a Gaussian filter followed by the Sobel operator for detecting the cracks as illustrated in Fig. 9(c). After filtering out the noise, the crack length on pixel level is calculated from the Euclidean distance of the grouped pixel points as a simulated crack length demonstrated in Fig. 9(d). Figs. 10 and 11 plot the measured crack length by the microscope, machinist scale and CV method showing strong agreement. Tables C.13 and C.14 in the Appendix, give full measurements of the recorded crack length as well as the crack length calculated by the computer vision method. In these tables, Error 1 compares the crack lengths on the front and back sides of the specimen measured by machinist scale and the microscope respectively. Error 2 indicates the difference between crack lengths measured by the microscope and CV method.

The crack length measured by the microscope and machinist scale has a relatively large error at 115 000 cycles in the second standard fatigue test, which could come from a local material inhomogeneity obstructing the growth of crack temporarily on one side. However, the rest measured crack lengths by the microscope and machinist scale have acceptable error indicating the cracks on the back and front sides are very similar, which makes the comparison of microscope and CV methods meaningful. Even though the difference between results of conventional and CV methods are relatively large at 200 000 cycles in the first test and 115 000

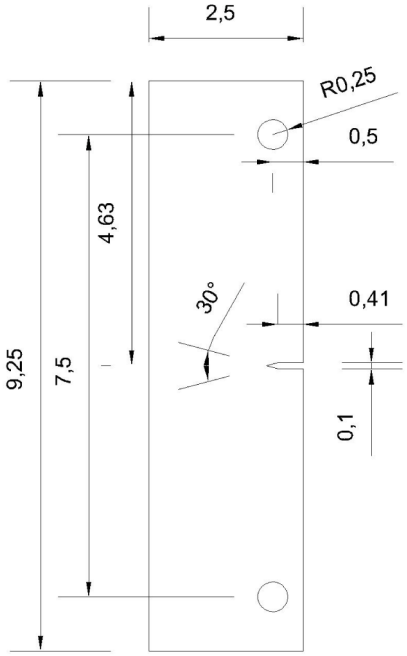

Fig. 7. Specimen plot of standard eccentrically-loaded single edge crack tension specimen, dimensions in inches.

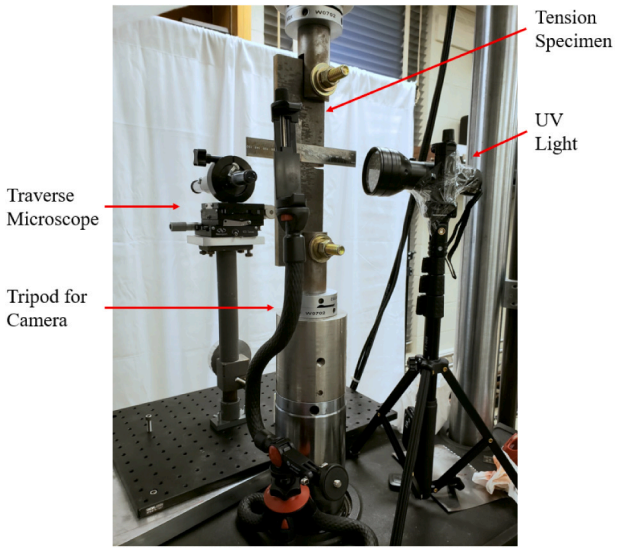

Fig. 8. Validation test setup for the computer vision method.

cycles in the second test, most measurements match very well with a mean of the error around 5.5% and standard deviation around 7.2%. The validation results demonstrate the performance of the developed CV method. Given the relative ease of the method, and its ability to quickly record the length of several cracks on the same specimen, it appears well suited for system fatigue tests where total crack length is a key experimental result.

2.2.4. Digital Image Correlation (DIC) method

DIC is a post-processing method to acquire the displacement and strain field of a structure under deformation. By looking for the characteristic strain field around a crack tip, DIC can be used for detecting the crack tip and calculating the crack length. Fig. 12 shows the procedure of applying the DIC method for crack detection used in this work. The first step is similar to the computer vision method, in that images are captured for analysis. The difference is that in order to perform correlation of images successfully,

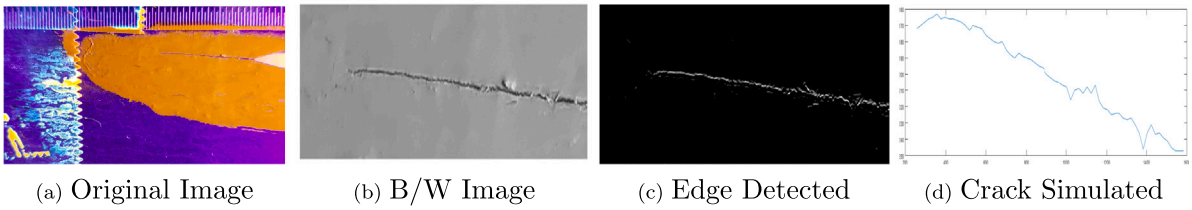

Fig. 9. The application of computer vision method.

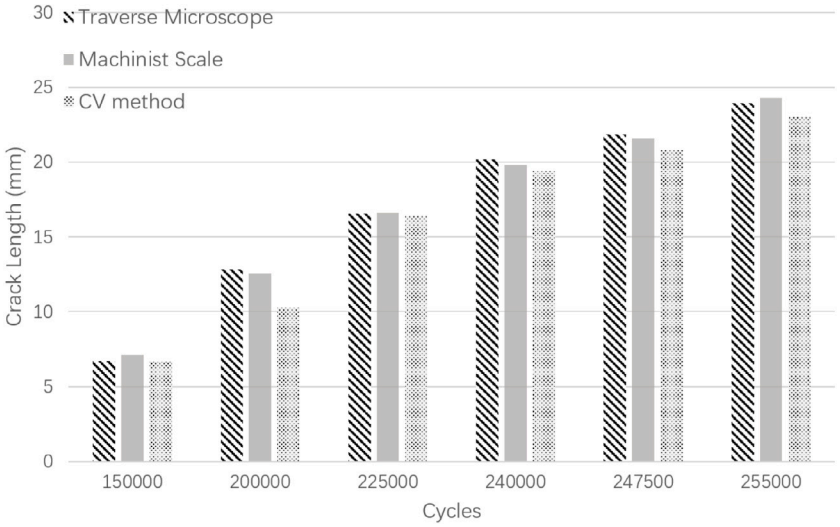

Fig. 10. Measured crack lengths of the first validation test.

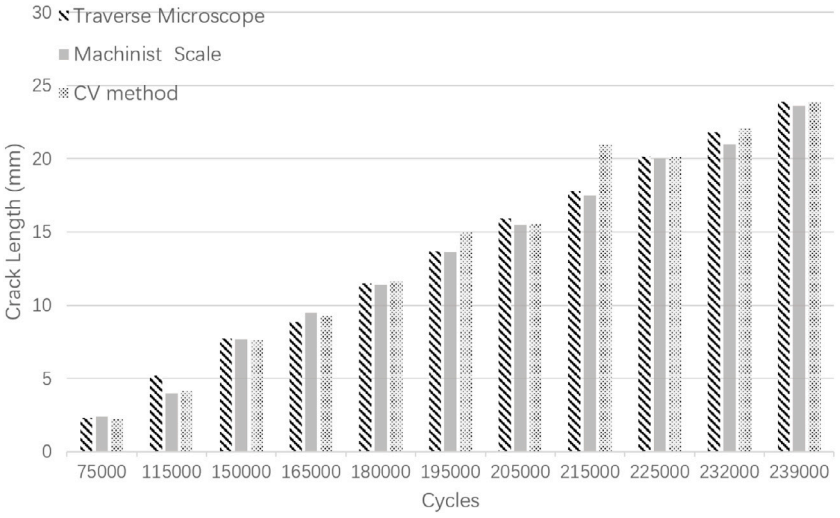

Fig. 11. Measured crack lengths of the second validation test.

the structure surface needs to be painted with a refined pattern, i.e. the surface is painted with black background color to which small white particles are added for tracking the displacement field. Then a region of interest (ROI) is drawn to indicate the area for analysis. The processing of the images is then performed by an open-source software named GOM Correlate, and the crack length can be acquired by plotting the major strain versus distance which is explained in detail in the following section.

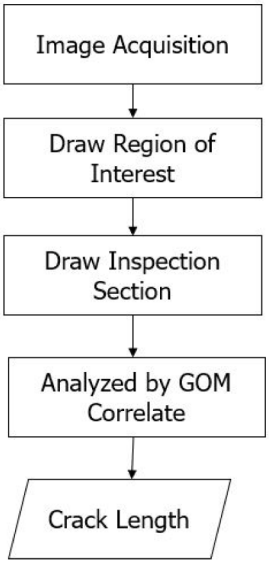

Fig. 12. Flow chart of DIC method.

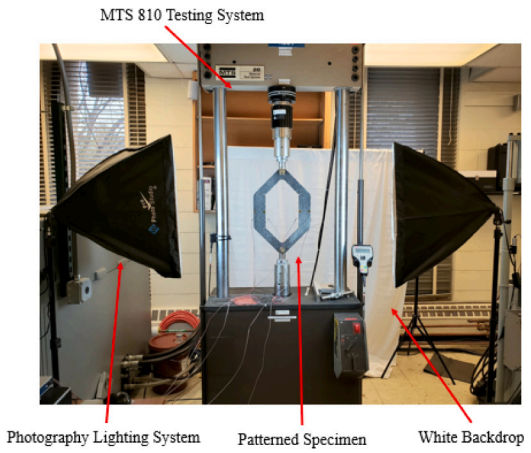

Fig. 13. Setup of DIC method (CCD camera is not included in this figure).

Image acquisition

The quality of the captured figure is critical for successful DIC, and this relies heavily on the camera and lighting system. A Blackfly BFLY-PGE-31S4M GigE Charge Coupled Device (CCD) camera manufactured by FLIR was used in the experiment. The reason for choosing CCD camera is that its sensors can create high-quality and low-noise images. A Sony IMX265 sensor is used in the Blackfly CCD camera, capturing monochrome images at 35 Frame per Second (FPS) with a resolution 2048 × 1536. A Tamron 23FM25SP lens is combined with the CCD camera, this is a 25 mm focal length lens, and on the hexagon specimens it can capture a figure around 10 cm × 8 cm area at a 26 cm objective distance. The camera was connected to a GigE host adapter with a RJ45 connector and controlled by a related piece of software named FlyCapture. In addition to the CCD camera system, a LimoStudio 700 W photography lighting system is chosen to provide high-quality and uniform light on the specimen. A white back drop hung behind the specimen for a clean background to help in the image analysis. The setup of the DIC system is shown in Fig. 13.

Dic analysis

The DIC analysis was performed by the GOM Correlate program. An image of the non-deformed specimen (reference image) and an image of the deformed specimen (current image) are input into the software. Within the image, a region of interest (ROI) is defined for the analysis. The analysis is performed on the ROI by cutting the reference image into small subsections and finding the corresponding locations in the current image. The movement between images is the displacement, and the corresponding strain field can then be calculated. After finishing the calculation and defining the inspection sections along the crack, a plot of major strain

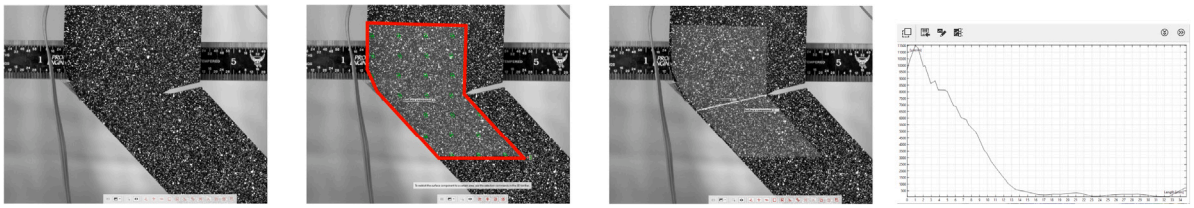

Fig. 14. The procedure for applying DIC method.

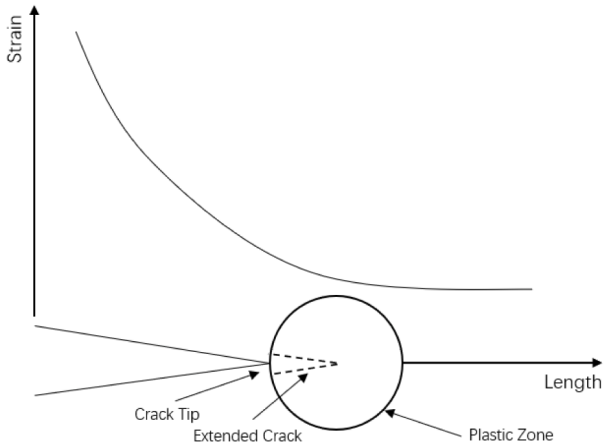

Fig. 15. Illustration of the change of major strain versus length.

versus length is generated for the defined sections. The length is scaled to the mm for determining crack length. The procedure is shown in Fig. 14. The major strain describes the strain from the tip of the EDM-machined precrack to the crack tip where it tends to have a turning point due to the plastic zone as illustrated in Fig. 15. In this figure, the strain reaches a plateau after the plastic zone with little change in strain with length. This transition was termed the turning point, and was associated with the plastic zone. By detecting this turning point, an approximation of the crack length can be made.

The plastic zone around the crack tip tends to extend the crack length determined by this method, resulting to a longer crack length than the actual crack length. Thus the crack length is corrected by subtracting the radius of the plastic zone. The radius of the plastic zone was estimated by Eq. (3), where K is the stress intensity factor and σ_y is the yield strength of the material. In order to simplify the calculation of the size of the plastic zone, two assumptions were made: (1) the size of the plastic zone is decreasing linearly with the increase of the number of cycles under a displacement control experiment; (2) the four cracks have the same size of plastic zone. The size of plastic zone before crack propagation is determined by calculating the stress intensity factor by Abaqus, while the size of the plastic zone after structure failure is assumed to be 0. Then a linear interpolation for the size of the plastic zone versus cycles can be determined. In this approach, the SIF is only calculated once to set up the initial plastic zone size. It should be noticed that the discussed DIC method is suitable for measuring the length of straight cracks that were seen in this experiment.

$$r_y = \frac{1}{2\pi}\left(\frac{K}{\sigma_y}\right)^2 \tag{3}$$

2.3. Strain measurement

Strain gauges were also employed in the fatigue test to capture strain in the specimen for a thorough understanding of the stress state in the experiment. The data from strain gauges can assist in the analysis of crack propagation by providing information on the strain and stress state in the specimens. The configuration of the data acquisition system as well as the setup of strain gauges are explained in the following sections.

Strain gauges and data acquisition system

OMEGA uni-axial strain gauges with 350 Ω resistance were employed in the hexagon tests. A quarter-bridge Wheatstone bridge setup was used for the gauges in this case, and a compensating strain gauge for the effect of temperature was not used since both the room temperature and specimen temperatures were stable during the 3–5 day time of these experiments. A National Instrument

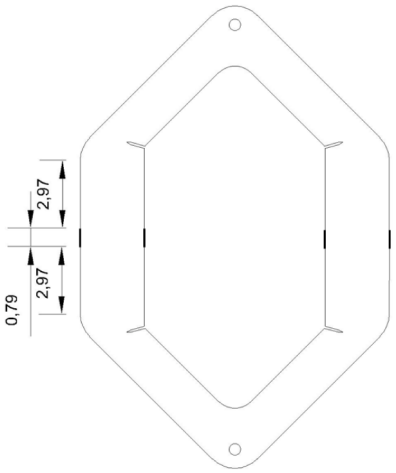

Fig. 16. Strain gauge locations.

measurement system containing NI 9236 and cDAQ-9181 were used to capture the strain data for these tests. NI 9236 is a 350 Ω, quarter bridge input module with 8 channels. cDAQ-9181 is a chassis with one slot capable to connect one NI 9236 modules to a computer via Ethernet. The system measures dynamic strain on all channels simultaneously allowing for synchronized, high-speed measurements. The data recording is controlled by a LabView algorithm, storing the strain by taking a 1 s sample every 20 s with 1000 Hz sample rate. The test frequency for this test was normally between 5 Hz and 7 Hz, so the 1 s sample time captured several complete load cycles.

Fig. 16 demonstrates the locations of the strain gauges. The strain gauges are glued on the center of each side of the vertical beams. The location is chosen to be away from the crack propagation area so that the crack tip strains would not impact the structural strains measured. In order to have a stable connection, the surface where strain gauges are glued on was machined flat via wire EDM at the same time the crack tips were cut.

3. Hexagon specimen experimental results and discussion

Five hexagon specimens have been tested, as outline in Table 1. The first three tests were primarily developmental, and focused on verifying the procedures for applying the computer vision method, the DIC method and the strain measurements. The last two hexagon tests used all of the developed methods simultaneously to record the crack growth. The following section discusses the testing results of the fifth hexagon specimen in detail; the results of other experiments are attached in Appendix. Additionally, full data sets for all tests, along with the first author's PhD thesis explaining the experimental results in greater detail have been archived electronically [26].

3.1. Fifth specimen crack growth results

The hexagon specimen was preloaded at 9.3 kN to guarantee a slack-free connection between the specimen and the fixture bolts. The MTS machine was set to a maximum displacement amplitude of 0.25 mm, with a resulting reaction force of 21.77 kN. The crack length was recorded every 100 000 cycles by pausing the test with just the preload applied, setting up the test apparatus, and then opening the crack by applying the maximum displacement. This opening was required for the CV and DIC method discussed below. In addition to the computer vision and DIC methods, a conventional machinist scale with markings of 0.5 mm was also used to provide a third method. This was also read with the crack opened at the specimen maximum displacement. Fig. 18(a) plots the propagation of the four cracks with respect to the number of applied cycles.

From the start of the test to 500 000 cycles, the four crack lengths have only minor differences owing to the symmetric design and identical starting length of the starter notches. However, with increasing cycles, the left bottom and right top cracks become dominant among the four cracks. At 867111 cycles, the right top crack has propagated through the width of the bar as demonstrated in Fig. 17. It can be observed from Fig. 18(a) that the left bottom crack is dominant on the left side while the right top crack is dominant on the right side. The maximum reaction force is recorded as shown in Fig. 18(b) which reflects a smooth decrease in rigidity from the beginning to a 800 000 cycles, followed by an abrupt drop with a steeper slope. The right top crack is broken at 867111 cycles resulting in a 1.33 kN maximum reaction force. Even if the maximum reaction force at the end of the test is small compared to that at the beginning, the specimen still has the capability to carry some load.

The experiment successfully simulated the dependence and interaction among components in deterioration with a structural redundancy mimicking the properties of complex marine structures. Notably, the emergence of a large crack in the left bottom and right top appears to shield the other crack on the corresponding side, slowing their growth. Full details of the recorded crack length and corresponding maximum reaction force are given in Table A.7.

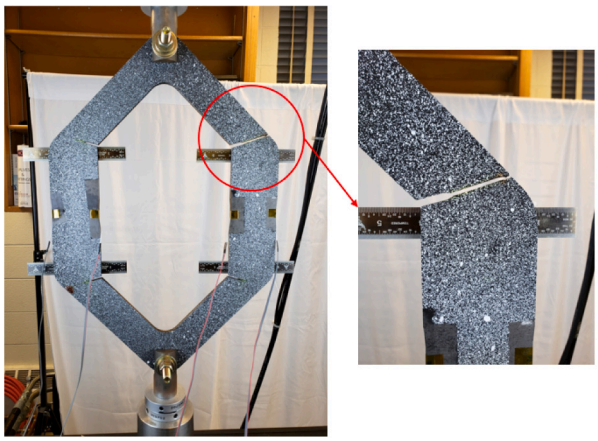

Fig. 17. Cracked hexagon specimen(backside).

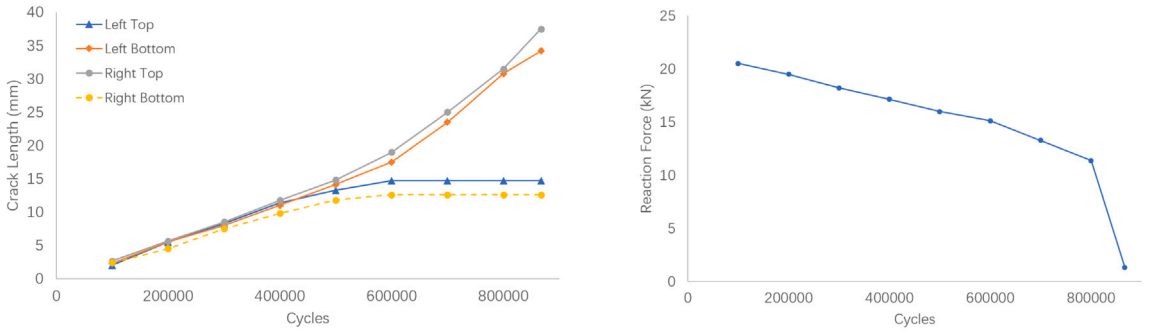

(a) Crack Length v.s. Cycles (b) Maximum Reaction Force v.s. Cycles

Fig. 18. Plot of crack length and maximum reaction force from the fifth experiment of hexagon specimen.

3.2. DIC and CV results for the fifth specimen

In addition to the machinist's scale, both the developed computer vision (CV) and the DIC method were applied to the fifth specimen. The DIC method requires an approximate plastic zone radius around the crack tip to determine the correct crack length. Fig. 19 shows the approximate correction radius used for the plastic zone. The stress intensity factor for the starter notch alone was simulated by Abaqus which leads to a plastic zone radius of 2.3 mm at the start of the experiment. The structure fails at 867111 cycles where the radius of the plastic zone is assumed to be 0. With the assumption that the radius of the plastic zone has a linear relation with applied cycles as discussed previously, the correction is calculated and applied to the DIC results. These results are shown in Fig. 20 and in Tables A.8 and A.9, where the crack length measured by machinist scale and DIC is compared followed by the percentage error. The CV result is also compared to the machinist measurement. The DIC and CV are implemented from 100 000 cycles to 800 000 cycles. It should be noted that the DIC and CV results of the left top and the right bottom at 800 000 cycles are not available since the crack cannot be opened owing to the size of the other cracks on the specimen at this point.

The percentage error is relatively large when the crack is small. With increasing crack growth, the percentage error decreases resulting in a mean error of 9.71% with a standard deviation of 7.36% for DIC method, a mean error of 4.23% with standard deviation of 3.98% for CV method. While the CV method tracks the machinist scale measurement more closely than the DIC method in this particular geometry, the errors from DIC are still relatively small, and the overall trend in crack length from DIC follows the results from the machinist scale very well as shown in Fig. 20. Thus, these results indicate that the DIC and CV method are both suitable for fatigue tests or monitoring of real world structures where crack length is a key factor. Additionally, for evaluating digital twins, having three sources of crack growth data with different fidelity is also useful.

3.3. Results of strain measurement

The strain gauge is deployed to understand the stress status of the hexagon specimen during the multi-crack degradation process. Each of the four strain gauges was configured as a quarter-bridge and measured the strain every 20 s with a 1000 Hz sample rate.

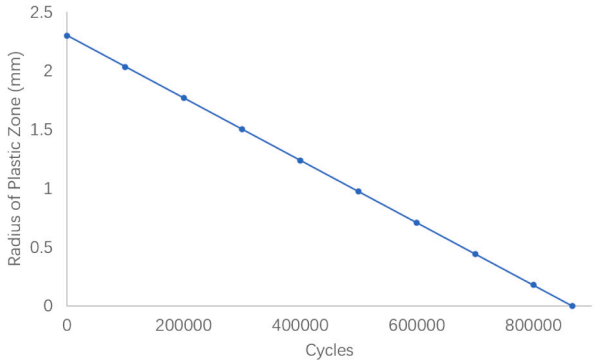

Fig. 19. Correction of radius of plastic zone.

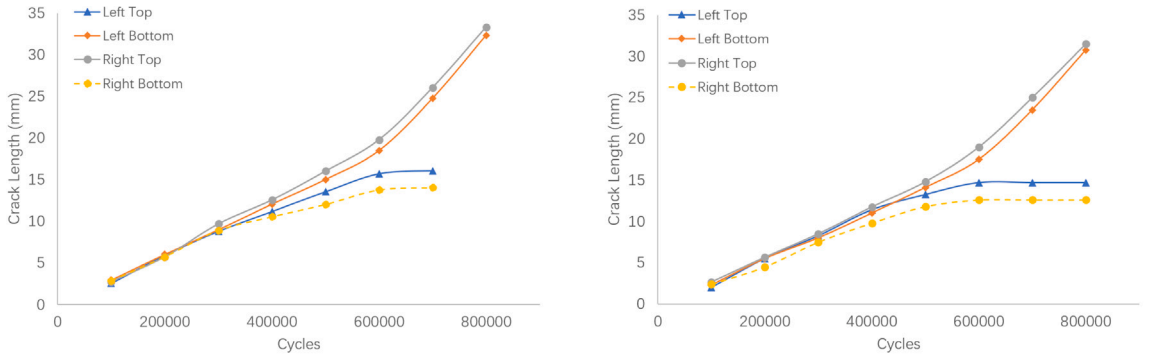

(a) Crack Length by DIC (b) Crack Length by Machinist Scale

Fig. 20. Comparison of crack length of the fifth hexagon experiment (Left: DIC, Right: Machinist Scale)

Table 2
Strain gauge locations.

Gauge no.	Location
0	Left Bar, Outside
1	Left Bar, Inside
2	Right Bar, Inside
3	Right Bar, Outside

The data is stored as text in a lvm file explored by Pandas Dataframe in Python. Due to the cyclic loading, the maximum strain corresponding to the maximum displacement is selected and extracted to monitor the status of the structure. With the extracted strain, the membrane and bending stress is calculated as well as the overall reaction force. Fig. 21 shows the strain of the fifth hexagon experiment with respect to the applied cycles. The numbering of the strain gauges is left-to-right across the specimen, as given in Table 2 and shown in Fig. 16.

Owing to the symmetric specimen design, strain 0 and strain 3 are increasing while strain 1 and strain 2 are decreasing with applied cycles; the bending and membrane stresses of the two beams are decreasing while bending stress has a larger slope compared to membrane stress. The bending stress decreases to 0 and starts to grow again around 740,000 cycles, which corresponds to the intersection of strain 0, 3 and strain 1, 2 in Fig. 21. This interesting phenomenon is illustrated in Fig. 24, where the arrow indicates the direction of the stress and the length of the arrow is proportional to the absolute value of the stress. Note that S_1 and S_2 in this figure refer to stress, not strains and the numbering does not correspond to the strain gauge numbering. Since the specimen has a symmetric design, Fig. 24 only shows the left beam of the hexagon specimen. From Fig. 24a to Fig. 24e, with the growth of cracks, S_1 is decreasing while S_2 is increasing. After S_2 becomes positive and keeps increasing, S_1 and S_2 are identical at a specific point resulting in pure membrane stress and the turning point of the bending stress in Fig. 22. Thus, a relationship between the stress distribution and crack size could be explored as part of a digital twin updating approach.

The total reaction force is calculated from the measured strains with the equivalent stress distribution integrated across the specimen and compared to the maximum reaction force indicated by the MTS testing system as shown in Fig. 23 which have similar trends and matches very well. The small difference could come from the fact that the reaction force recorded by the MTS testing system is a static force, i.e. the test is stopped and the maximum displacement is applied to record the maximum reaction force,

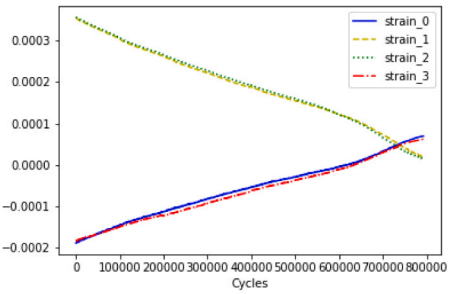

Fig. 21. Measured maximum strain of the fifth hexagon experiment.

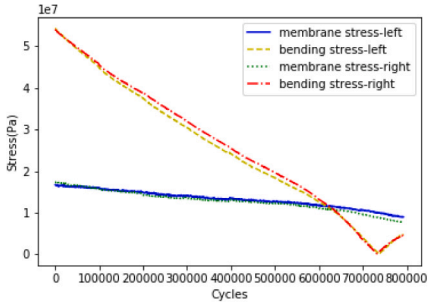

Fig. 22. Maximum membrane and bending stress of the fifth hexagon experiment.

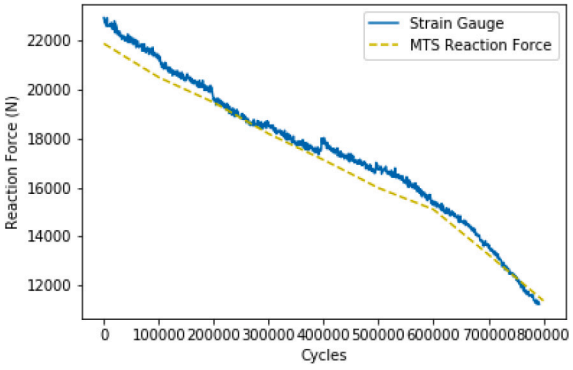

Fig. 23. Comparison of reaction force.

while the strain gauge measurement indicates the dynamic force during the experiment. The measured strain shown in Table B.12 is the average strain on a 4 min period around each measuring points of crack growth measurement. The strain gauges successfully monitor the complex change inside the hexagon specimen during the experiment, and provide another data source that could be used in the assessment of digital twins attempting to perform prognosis on the structure independent of direction measurements of crack length.

4. Conclusion

As digital twins move towards predicting system-level performance for marine structures, evaluating these twin approaches with real-world data becomes challenging. In this work, a small, displacement-controlled, four-crack laboratory specimen was developed to mimic many of the characteristics of larger marine structural systems. Five different hexagon specimens were tested, three development specimens, and two specimens with all data collection methods applied. A new computer vision method for making rapid crack length measurements for specimens such as this one was also developed and initially validated as part of this work. This method provided rapid crack length determination without the need to apply complex DIC speckle patterns and can work from a single image.

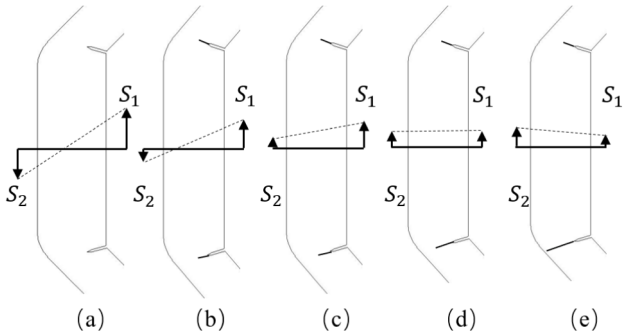

Fig. 24. Analysis of stress change over the experiment.

For the final two specimens, 18 different variables were recorded over time, the number of applied cycles, the maximum reaction force of the specimen, each crack size by machinist scale, each crack size by a computer vision method, each crack size by a DIC method, and structural strains at four locations. The measurement methods were in close agreement overall, and provide a consistent data set for the community. This data set has also been archived electronically at the University of Michigan. This comprehensive data set can be used by future authors to evaluate the ability of digital twins to make system level prognosis.

Acknowledgments

This work was supported by Dr. Paul Hess of the Office of Naval Research, Department of the Navy, United States Government, Code 331 under grant N00014-16-1-2978. The authors appreciate the support given by the Marine Structures Design Laboratory (MSDL) of the University of Michigan and the help from Professor John Allison, John Lasecki, Fatigue Testing Laboratory of the Materials Science and Engineering Department at the University of Michigan where the tests were conducted.

Appendix A. Test results of hexagon specimens

The following is the crack length and corresponding maximum reaction force from the first hexagon specimen to the fourth hexagon specimen. The crack length is measured by machinist scale, CV method and DIC method as marked in the tables below. It should be noted that since the first test is for verifying the design, the records are not complete. Additionally, full experimental details and data sets have been archived in the University of Michigan Library's archive service Deep Blue in the first author's PhD Thesis [26], and the corresponding data repository https://doi.org/10.7302/e3n8-wa61.

A.1. Specimen 1

See Table A.3.

Table A.3
Recorded crack length of the first experiment of hexagon specimen (unit: Length mm; Force kN; MS = Machinist Scale; DIC = Digital Image Correlation; CV = Computer Vision).

Cycles	Left top (MS)	Left bottom (MS)	Right top (MS)	Right bottom (MS)	Maximum reaction force
369706	2.50	4.00	4.00	5.50	21.22
569706	10.80	11.80	9.50	11.80	19.14
669706	14.20	14.50	12.50	16.00	17.89
769706	17.00	16.80	13.60	19.40	17.01
869706	21.10	18.00	14.00	24.00	15.28

A.2. Specimen 2

See Table A.4.

A.3. Specimen 3

See Table A.5.

A.4. Specimen 4

See Table A.6.

Table A.4
Recorded crack length of the second experiment of hexagon specimen (unit: Length mm; Force kN; MS = Machinist Scale; DIC = Digital Image Correlation; CV = Computer Vision; MRF = Maximum Reaction Force).

Cycles	Left top (MS;DIC;CV)	Error %	Left bottom (MS;DIC;CV)	Error %	Right top (MS;DIC;CV)	Error %	Right bottom (MS;DIC;CV)	Error %	MRF
100000	2.25;2.89;2.12	28.52;5.77	2.20;3.09;1.68	40.53;23.64	2.50;2.19;N/A	12.33;N/A	2.25;2.59;N/A	15.18;N/A	20.02
200000	5.40;5.58 ;4.77	3.40;11.67	5.40;6.28;4.60	16.36;14.81	5.40;6.58;5.01	21.91;7.22	4.70;5.58;4.22	18.79;10.21	19.36
300000	8.00;8.27 ;7.38	3.44;7.75	8.30;8.67;7.25	10.20;12.65	8.70;8.48;7.43	2.59;14.60	8.00;8.87;6.05	10.94;24.38	17.73
400000	10.90;10.97;10.16	0.61;6.79	11.50;11.77;10.01	2.32;12.96	11.30;10.97;9.22	2.95;18.40	10.50;11.07;9.06	5.40;13.71	17.04
500000	13.60;13.26;12.65	2.51;6.99	14.00;14.06;12.49	0.42;10.79	12.50;12.86;12.38	2.87;0.96	12.40;12.96;11.75	4.50;5.24	16.35
600000	15.30;14.05;14.42	8.17;5.75	15.70;16.05;15.20	2.23;3.18	14.20;14.35;13.08	1.06;7.89	14.30;15.85;13.53	10.84;5.38	15.85
700000	16.40;16.54;17.86	0.86;8.90	18.20;18.04;18.52	0.87;1.76	14.90;16.04;16.40	7.66;10.07	16.00;17.24;14.62	7.76;8.63	15.48
800000	17.20;17.23;16.12	0.19;6.28	20.00;20.83;20.93	4.17;4.65	15.50;16.63;15.19	7.31;2.00	17.10;20.03;16.60	17.15;2.92	15.06
900000	17.50;18.42;19.06	5.29;8.91	23.40;23.92;22.06	2.24;5.73	15.50;17.43;13.65	12.42;11.94	18.90;20.63;18.53	9.13;1.96	14.98
1000000	17.50;18.62;N/A	6.38;N/A	27.30;28.42;27.84	4.09;1.98	15.50;17.62;N/A	13.65;N/A	20.00;20.92;N/A	4.58;N/A	14.13
1100000	17.70;N/A;N/A	N/A;N/A	32.50;33.31;31.95	2.49;1.69	17.00;18.81;N/A	10.64;N/A	21.20;21.81;N/A	2.87;N/A	13.86
1147505	18.00;N/A;N/A	N/A;N/A	36.00;N/A;N/A	N/A;N/A	17.50;N/A;N/A	N/A;N/A	21.50;N/A;N/A	N/A;N/A	10.64
1200000	18.00;N/A;N/A	N/A;N/A	37.50;N/A;N/A	N/A;N/A	17.50;N/A;N/A	N/A;N/A	21.50;N/A;N/A	N/A;N/A	1.9
Mean of Error % (DIC;CV)			7.96;8.56						
Std of Error % (DIC;CV)			8.08;5.67						

Table A.5
Recorded crack length of the third experiment of hexagon specimen (unit: Length mm; Force kN; MS = Machinist Scale; DIC = Digital Image Correlation; CV = Computer Vision).

Cycles	Left top	Left bottom	Right top	Right bottom	Maximum reaction force
100000	2.50	2.50	2.50	2.50	21.91
200000	4.50	5.00	5.00	4.50	21.34
300000	7.00	9.00	9.00	6.60	20.03
400000	9.20	12.30	13.20	8.30	18.36
500000	9.20	17.50	18.30	8.90	17.32
600000	9.20	24.40	25.70	9.20	14.72
700000	9.20	31.80	31.80	9.50	12.04

Table A.6
Comparison of crack length of machinist scale and dic method of the fourth hexagon experiment (unit: Length mm; Force kN; MS = Machinist Scale; DIC = Digital Image Correlation; CV = Computer Vision; MRF = Maximum Reaction Force).

Cycles	Left top (MS;DIC;CV)	Error %	Left bottom (MS;DIC;CV)	Error %	Right top (MS;DIC;CV)	Error %	Right bottom (MS;DIC;CV)	Error %	MRF
100000	2.00;2.48;1.48	24.14;26	2.00;2.78;1.91	39.14;4.26	2.00;2.68;1.69	34.14;15.5	1.90;2.58;1.83	35.94;3.68	20.81
200000	4.50;4.46;4.68	0.76;4	4.70;4.86;4.72	3.52;0.42	5.20;4.76;4.88	8.35;6.15	4.50;4.96;4.19	10.35;6.88	19.57
300000	7.60;7.17;7.56	5.94;0.52	8.50;7.95;7.8	6.48;8.23	8.10;6.85;7.57	15.45;6.54	7.10;6.54;7.03	7.76;0.98	18.87
400000	9.80;9.83;9.89	0.32;0.92	11.40;11.03;10.73	3.23;5.88	11.40;10.83;11.37	4.98;0.26	9.50;9.83;9.55	3.49;0.53	17.61
500000	11.60;12.61;10.96	8.74;5.52	15.40;14.71;14.81	4.45;3.83	14.30;14.61;14.63	2.19;2.31	11.50;12.11;10.13	5.34;11.91	16.74
600000	12.20;13.69;12.12	12.27;0.65	18.50;17.70;19.04	4.34;2.92	18.60;17.90;19.30	3.77;3.76	12.60;13.89;11.73	10.29;11.91	15.33
700000	12.20;13.98;N/A	14.59;N/A	26.80;24.88;24.29	7.16;9.36	26.30;25.28;25.95	3.87;1.33	12.60;14.18;N/A	12.54;N/A	13.24
800000	12.20;N/A;N/A	N/A;N/A	33.50;33.96;35.8	1.38;6.86	33.00;33.46;30.2	1.40;8.48	12.60;N/A;N/A	N/A;N/A	10.37
813097	12.20;N/A;N/A	N/A;N/A	37.50;N/A;N/A	N/A;N/A	33.00;N/A;N/A	N/A;N/A	12.60;N/A;N/A	N/A;N/A	1.31
Mean of Error % (DIC;CV)			9.88;5.52						
Std of Error % (DIC;CV)			10.19;5.39						

A.5. Specimen 5

See Tables A.7–A.9.

Table A.7
Recorded crack length and reaction force of the fifth experiment of hexagon specimen, machinist's scale used for length.

Cycles	Left top mm	Left bottom mm	Right top mm	Right bottom mm	Maximum reaction force kN
100000	2.00	2.30	2.65	2.40	20.51
200000	5.50	5.50	5.65	4.50	19.48
300000	8.25	8.00	8.50	7.50	18.2
400000	11.40	11.00	11.75	9.80	17.13
500000	13.25	14.10	14.80	11.80	15.99
600000	14.70	17.50	19.00	12.60	15.11
700000	14.70	23.50	25.00	12.60	13.27
800000	14.70	30.75	31.50	12.60	11.38
867111	14.70	34.20	37.50	12.60	1.33

Appendix B. Results of strain measurement

The following appendix shows the results of strain measurement of the third and fourth hexagon experiment including measured strain, calculated membrane and bending stress and the comparison of reaction force. Since the strain gauge measures small surface area (3 mm × 2 mm), it can be affected by surface impurities easily. In the fourth test, we believe the measurement of strain gauge 2 is influenced by surface impurity or a poor connection to the specimen, possibly from the DIC speckle pattern, resulting in the

Table A.8
Comparison of left side crack lengths by machinist scale, DIC method and CV method of the fifth hexagon experiment (unit: mm; MS = Machinist Scale; DIC = Digital Image Correlation; CV = Computer Vision).

Cycles	Left top (MS;DIC;CV)	Error % (DIC;CV)	Left bottom (MS;DIC;CV)	Error % (DIC;CV)
100000	2.00;2.56;2.27	28.26;13.50	2.30;2.96;2.19	28.92;4.78
200000	5.50;5.93;5.51	7.82;0.18	5.50;6.03;5.22	9.64;5.09
300000	8.25;8.80;8.38	6.61;1.57	8.00;8.99;7.79	12.44;2.63
400000	11.40;11.16;11.12	2.09;2.46	11.00;12.06;11.89	9.64;8.09
500000	13.25;13.53;12.8	2.08;3.40	14.10;15.03;13.98	6.56;0.85
600000	14.70;15.69;15.29	6.74;4.01	17.50;18.49;18.97	5.66;8.4
700000	14.70;16.06;16	9.23;8.84	23.50;24.76;22.93	5.34;2.42
800000	14.70;N/A;N/A	N/A;N/A	30.75;32.32;31.92	5.11;3.80

Table A.9
Comparison of right side crack lengths by machinist scale, DIC method and CV method of the fifth hexagon experiment (unit: mm; MS = Machinist Scale; DIC = Digital Image Correlation; CV = Computer Vision).

Cycles	Right top (MS;DIC;CV)	Error % (DIC;CV)	Right bottom (MS;DIC;CV)	Error % (DIC;CV)
100000	2.65;2.76;2.42	4.34;8.68	2.40;2.86;2.81	19.38;17.08
200000	5.65;5.73;5.34	1.42;5.49	4.50;5.73;4.43	27.34;1.55
300000	8.50;9.69;8.38	14.06;1.41	7.50;8.89;7.41	18.60;1.2
400000	11.75;12.56;11.88	6.90;1.11	9.80;10.56;9.81	7.76;0.10
500000	14.80;16.02;14.5	8.28;2.03	11.80;12.02;11.69	1.91;0.93
600000	19.00;19.79;17.9	4.16;5.79	12.60;13.79;12.53	9.45;0.55
700000	25.00;26.06;26.14	4.22;4.56	12.60;14.05;N/A	11.56,N/A
800000	31.50;33.32;32.16	5.78;2.09	12.60;N/A;N/A	N/A;N/A

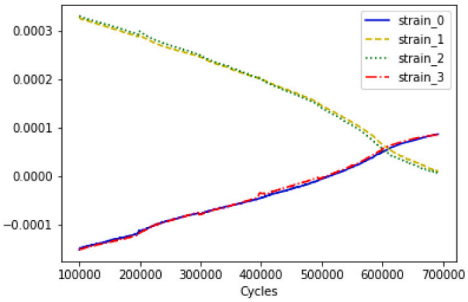

Fig. B.25. Measured strain of the third hexagon experiment.

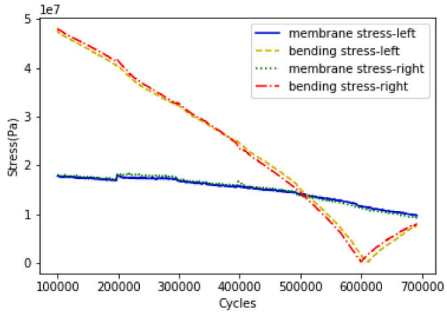

Fig. B.26. Membrane and bending stress of the third hexagon experiment.

difference compared with strain 1 and the gap between reaction forces from integrating strains and that measured by the MTS machine.

B.1. Third specimen results

See Figs. B.25, B.26 and B.27 and Table B.10.

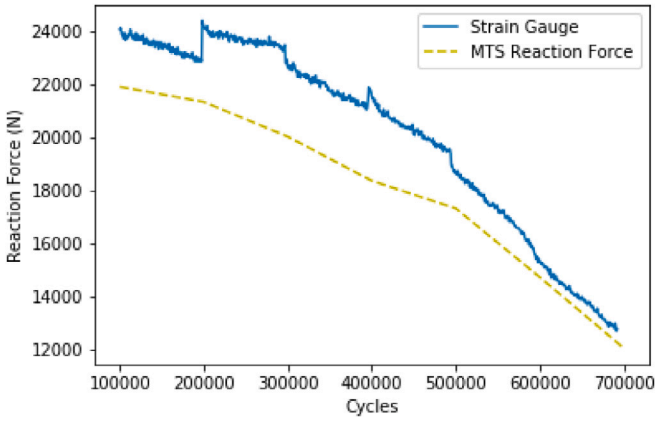

Fig. B.27. Comparison of reaction force of the third hexagon experiment.

Table B.10
Maximum strain at each measuring points for the third hexagon experiment.

Cycles	Strain 0	Strain 1	Strain 2	Strain 3
100000	−1.49e−04	3.27e−04	3.30e−04	−1.50e−04
200000	−1.12e−04	2.90e−04	2.98e−04	−1.16e−04
300000	−7.73e−05	2.45e−04	2.47e−04	−7.83e−05
400000	−4.43e−05	2.00e−04	1.99e−04	−3.51e−05
500000	−5.09e−06	1.46e−04	1.40e−04	−3.55e−06
600000	5.04e−05	6.53e−05	5.56e−05	5.61e−05
700000	8.66e−05	1.06e−05	6.84e−06	8.58e−05

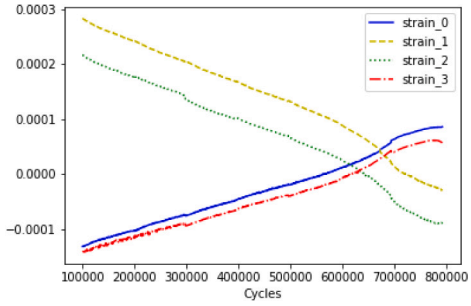

Fig. B.28. Measured strain of the fourth hexagon experiment.

B.2. Fourth specimen results

See Figs. B.28, B.29 and B.30 and Table B.11.

B.3. Fifth specimen results

See Table B.12.

Appendix C. Results of standard fatigue specimens

See Tables C.13 and C.14.

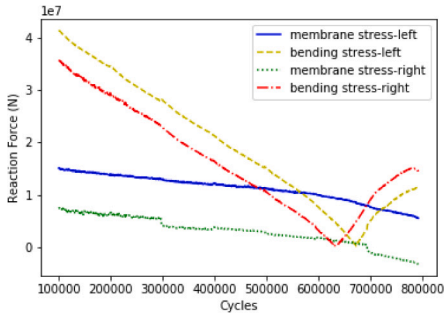

Fig. B.29. Membrane and bending stress of the fourth hexagon experiment.

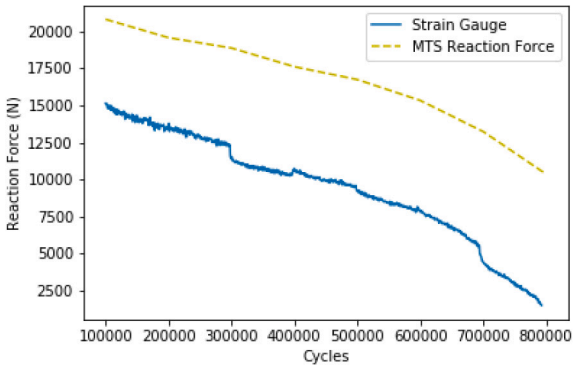

Fig. B.30. Comparison of reaction force of the fourth hexagon experiment.

Table B.11
Maximum strain at each measuring points for the fourth hexagon experiment.

Cycles	Strain 0	Strain 1	Strain 2	Strain 3
100000	−1.32e−04	2.82e−04	2.16e−04	−1.41e−04
200000	−1.03e−04	2.42e−04	1.79e−04	−1.12e−04
300000	−7.57e−05	2.05e−04	1.35e−04	−9.40e−05
400000	−4.55e−05	1.67e−04	1.00e−04	−6.32e−05
500000	−1.99e−05	1.31e−04	6.55e−05	−3.97e−05
600000	1.12e−05	8.80e−05	2.50e−05	−7.39e−06
700000	6.29e−05	1.35e−05	−5.02e−05	3.94e−05
800000	8.52e−05	−2.95e−05	−8.91e−05	5.70e−05

Table B.12
Maximum strains at each measuring point for the fifth hexagon experiment.

Cycles	Strain 0	Strain 1	Strain 2	Strain 3
100000	−1.44e−04	3.04e−04	3.06e−04	−1.48e−04
200000	−1.12e−04	2.62e−04	2.65e−04	−1.22e−04
300000	−8.15e−05	2.23e−04	2.27e−04	−9.25e−05
400000	−5.31e−05	1.88e−04	1.93e−04	−6.08e−05
500000	−2.87e−05	1.55e−04	1.60e−04	−3.67e−05
600000	−4.26e−06	1.22e−04	1.21e−04	−1.09e−05
700000	3.31e−05	7.34e−05	6.59e−05	2.99e−05
800000	6.95e−05	2.11e−05	1.54e−05	6.21e−05

Table C.13
Validation results of computer vision based method from the first standard fatigue test (unit: mm).

Cycles	Microscope (back)	Machinist scale (front)	CV method (front)	Error1 (%)	Error2 (%)
150000	6.7	7.1	6.7	5.9	0.4
200000	12.8	12.5	10.3	2.4	19.8
225000	16.6	16.6	16.4	0.2	1.0
240000	20.2	19.8	19.4	1.8	4.0
247500	21.8	21.6	20.8	1.1	4.8
255000	23.9	24.3	23.0	1.6	3.9
Mean of error				2.2	5.6
Std of error				2.0	7.2

Table C.14
Validation results of computer vision based method from the second standard fatigue test (unit: mm).

Cycles	Traverse microscope (back)	Machinist scale (front)	CV method (front)	Error1 (%)	Error2 (%)
75000	2.3	2.4	2.2	5.0	1.8
115000	5.2	4.0	4.1	22.8	20.2
150000	7.7	7.6	7.6	1.3	1.2
165000	8.9	9.5	9.3	6.9	4.4
180000	11.5	11.4	11.7	0.9	1.6
195000	13.7	13.6	15.0	0.5	9.9
205000	15.9	15.5	15.5	2.6	2.3
215000	17.8	17.5	21.0	1.6	17.9
225000	20.2	20.0	20.1	0.8	0.3
232000	21.8	21.0	22.1	3.6	1.4
239000	23.9	23.6	23.9	1.2	0.16
Mean of error				4.3	5.5
Std of error				6.5	7.2

References

[1] Moan T. Integrity management of offshore structures with emphasis on design for structural damage tolerance. J Offshore Mech Arct Eng 2020;142(3). http://dx.doi.org/10.1115/1.4045373, 031104 (15 pages).

[2] Zou G, González A, Banisoleiman K, Faber MH. An integrated probabilistic approach for optimum maintenance of fatigue-critical structural components. 68: 102649. http://dx.doi.org/10.1016/j.marstruc.2019.102649.

[3] Lotsberg I, Sigurdsson G, Fjeldstad A, Moan T. Probabilistic methods for planning of inspection for fatigue cracks in offshore structures. Mar Struct 2016;46:167–92. http://dx.doi.org/10.1016/j.marstruc.2016.02.002.

[4] Abbas M, Shafiee M. An overview of maintenance management strategies for corroded steel structures in extreme marine environments. Mar Struct 2020;71:102718. http://dx.doi.org/10.1016/j.marstruc.2020.102718.

[5] Straub D. Stochastic modeling of deterioration processes through dynamic Bayesian networks. J Eng Mech 2009;135(10):1089. http://dx.doi.org/10.1061/(ASCE)EM.1943-7889.0000024.

[6] Zhu J, Collette M. Updating structural engineering models with in-service data: approaches and implications for the naval community. Naval Eng J 2015;127(1):63–74.

[7] Zhu J, Collette M. A Bayesian approach for shipboard lifetime wave load spectrum updating. Struct Infrastruct Eng 2017;13(2):298–312. http://dx.doi.org/10.1080/15732479.2016.1165709.

[8] Luque J, Straub D. Reliability analysis and updating of deteriorating systems with dynamic Bayesian networks. Struct Saf 2016;62:34–46. http://dx.doi.org/10.1016/j.strusafe.2016.03.004.

[9] Luque J, Straub D. Risk-based optimal inspection strategies for structural systems using dynamic Bayesian networks. Struct Saf 2019;76:68–80. http://dx.doi.org/10.1016/j.strusafe.2018.08.002.

[10] Cai B, Shao X, Liu Y, Kong X, Wang H, Xu H, Ge W. Remaining useful life estimation of structure systems under the influence of multiple causes: subsea pipelines as a case study. IEEE Trans Ind Electron 2020;67(7):5737–47. http://dx.doi.org/10.1109/TIE.2019.2931491.

[11] Liu Y, Frangopol DM, Cheng M. Risk-informed structural repair decision making for service life extension of aging naval ships. Mar Struct 2019;64:305–21. http://dx.doi.org/10.1016/j.marstruc.2018.10.008.

[12] Gordo JM, Soares CG. Compressive tests on short continuous panels. Mar Struct 2008;21(2–3):113–37. http://dx.doi.org/10.1016/j.marstruc.2007.12.005.

[13] Xu MC, Soares CG. Experimental study on the collapse strength of wide stiffened panels. Mar Struct 2013;30:33–62. http://dx.doi.org/10.1016/j.marstruc.2012.10.003.

[14] Saad-Eldeen S, Garbatov Y, Soares CG. Experimental strength analysis of steel plates with a large circular opening accounting for corrosion degradation and cracks subjected to compressive load along the short edges. Mar Struct 2016;48:52–67. http://dx.doi.org/10.1016/j.marstruc.2016.05.001.

[15] Saad-Eldeen S, Garbatov Y, Soares CG. Ultimate strength analysis of highly damaged plates. Mar Struct 2016;45:63–85. http://dx.doi.org/10.1016/j.marstruc.2015.10.006.

[16] Garbatov Y, Soares CG. Uncertainty assessment of fatigue damage of welded ship structural joints. Eng Struct 2012;44:322–33. http://dx.doi.org/10.1016/j.engstruct.2012.06.004.

[17] Saad-Eldeen S, Garbatov Y, Guedes Soares C. Experimental assessment of corroded steel box-girders subjected to uniform bending. Ships Offshore Struct 2013;8(6):653–62. http://dx.doi.org/10.1080/17445302.2012.718171.

[18] Saad-Eldeen S, Garbatov Y, Soares CG. Effect of corrosion degradation on ultimate strength of steel box girders. Corros Eng, Sci Technol 2012;47(4):272–83. http://dx.doi.org/10.1179/1743278212Y.0000000005.

[19] Pang JHL, Hoh HJ, Tsang KS, Low J, Kong SC, Yuan WG. Fatigue crack propagation analysis for multiple weld toe cracks in cut-out fatigue test specimens from a girth welded pipe. 94: 158–165. http://dx.doi.org/10.1016/j.ijfatigue.2016.09.011.

[20] Anis SF, Koyama M, Hamada S, Noguchi H. Simplified stress field determination for an inclined crack and interaction between two cracks under tension. 107: 102561. http://dx.doi.org/10.1016/j.tafmec.2020.102561.
[21] Sun W, Zhu Y, Huo J-Z, Chen X-H. Multiple cracks failure rule for TBM cutterhead based on three-dimensional crack propagation calculation. 93: 224–240. http://dx.doi.org/10.1016/j.engfailanal.2018.07.002.
[22] Soares CG, Garbatov Y. Reliability of corrosion protected and maintained ship hulls subjected to corrosion and fatigue. 43(2): 65–78.
[23] Okawa T, Sumi Y, Mohri M. Simulation-Based fatigue crack management of ship structural details applied to longitudinal and transverse connections. 19(4): 217–240. http://dx.doi.org/10.1016/j.marstruc.2007.01.002.
[24] Huang W, Garbatov Y, Guedes Soares C. Fatigue reliability assessment of correlated welded web-frame joints. J Mar Sci Appl (China); 13(1); 23–31. http://dx.doi.org/10.1007/s11804-014-1228-z.
[25] Huang W, Sridhar N. Fatigue failure risk assessment for a maintained stiffener-frame welded structure with multiple site cracks. 08(02): 1650024. http://dx.doi.org/10.1142/S1758825116500241.
[26] Zhang K. Development and experimental validation of dynamic bayesian networks for system reliability prediction. Ph.D. thesis, University of Michigan. Ann Arbor, MI; 2020, URL http://hdl.handle.net/2027.42/155231.
[27] Saenz EE, Carlsson LA, Salivar GC, Karlsson AM. Fatigue crack propagation in polyvinylchloride and polyethersulfone polymer foams. J Sandw Struct Mater 2014;16(1):42–65.
[28] Resch M, Nelson D, Yuce H, Ramusat G. A surface acoustic wave technique for monitoring the growth behavior of small surface fatigue cracks. J Nondestruct Eval 1985;5(1):1–7.
[29] Kimoto K, Ueno S, Hirose S. Image-based sizing of surface-breaking cracks by SH-wave array ultrasonic testing. Ultrasonics 2006;45(1–4):152–64.
[30] Longo R, Vanlanduit S, Vanherzeele J, Guillaume P. A method for crack sizing using laser doppler vibrometer measurements of surface acoustic waves. Ultrasonics 2010;50(1):76–80.
[31] Prasanna P, Dana K, Gucunski N, Basily B. Computer-vision based crack detection and analysis. In: Sensors and smart structures technologies for civil, mechanical, and aerospace systems 2012. 8345, International Society for Optics and Photonics; 2012, 834542.
[32] Lattanzi D, Miller GR. Robust automated concrete damage detection algorithms for field applications. J Comput Civ Eng 2012;28(2):253–62.
[33] Jahanshahi MR, Masri SF. Adaptive vision-based crack detection using 3D scene reconstruction for condition assessment of structures. Autom Constr 2012;22:567–76.
[34] Torok MM, Golparvar-Fard M, Kochersberger KB. Image-based automated 3D crack detection for post-disaster building assessment. J Comput Civ Eng 2013;28(5):A4014004.
[35] Oh J-K, Jang G, Oh S, Lee JH, Yi B-J, Moon YS, Lee JS, Choi Y. Bridge inspection robot system with machine vision. Autom Constr 2009;18(7):929–41.
[36] Koch C, Paal SG, Rashidi A, Zhu Z, K̀onig M, Brilakis I. Achievements and challenges in machine vision-based inspection of large concrete structures. Adv Struct Eng 2014;17(3):303–18.
[37] Yates J, Zanganeh M, Tai Y. Quantifying crack tip displacement fields with DIC. Eng Fract Mech 2010;77(11):2063–76.
[38] Mokhtarishirazabad M, Lopez-Crespo P, Moreno B, Lopez-Moreno A, Zanganeh M. Evaluation of crack-tip fields from dic data: a parametric study. Int J Fatigue 2016;89:11–9.
[39] Abanto-Bueno J, Lambros J. Investigation of crack growth in functionally graded materials using digital image correlation. Eng Fract Mech 2002;69(14–16):1695–711.
[40] Nixon M, Aguado AS. Feature extraction and image processing for computer vision. Academic Press; 2012.
[41] Shapiro LG, Stockman G. Computer vision: Theory and applications. Prentice Hall; 2001.
[42] ASTM. ASTM E647 Standard test method for measurement of fatigue crack growth rates. ASTM International; 2011.